Materials Characterization 216 (2024) 114228

Contents lists available at ScienceDirect

Materials Characterization

journal homepage: www.elsevier.com/locate/matchar

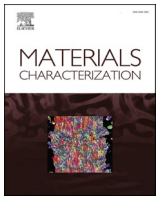

Microstructural investigation of nanocrystalline Nd-Fe-B magnets fabricated by laser powder bed fusion

Ho-Jeong Kim [a], Ye Ryeong Jang [a], Hyun-Sook Lee [a], Jung-Wook Cho [b], Taesuk Jang [c], Du-Rim Eo [d,*], Wooyoung Lee [a,*]

[a] Department of Materials Science and Engineering, Yonsei University, 50 Yonsei-ro, Seoul, Republic of Korea
[b] Graduate Institute of Ferrous & Eco Materials Technology, Pohang University of Science and Technology (POSTECH), 77 Cheongam-ro, Pohang, Republic of Korea
[c] Department of Advanced Materials Engineering, Sunmoon University, Asan 336-708, Republic of Korea
[d] Customized Manufacturing R&D Department, Korea Institute of Industrial Technology (KITECH), 113-58 Seohaean-ro, Siheung, Republic of Korea

ARTICLE INFO

Keywords:
Additive manufacturing
Nd-Fe-B
Permanent magnet
Laser powder bed fusion
Solidification
Amorphous phase

ABSTRACT

Nd-Fe-B magnets were manufactured by laser powder bed fusion (LPBF) using commercially available spherical powder (MQP-S-11-9). The magnets were manufactured at four different volume energy densities but similar relative densities to investigate the relations between the process, structure, and characteristics. Unlike the nanocomposite microstructure of the initial powder, the microstructure of the LPBF samples had (Nd, Pr)$_2$Fe$_{14}$B grains separated by grain boundary phases through the remelting and solidification of the initial powder. The cooling rate of the melt pool increased as the volume energy density decreased, suppressing the crystallization of α-Fe in the grain boundary phase. When the volume energy density was less than 86 J/mm^3, the crystallization of α-Fe was fully suppressed, and the grain boundary phases became amorphous, resulting in higher coercivity than that of the initial powder. The magnet with the strongest magnetic properties of H_{ci} = 10.3 kOe, B_r = 6.2 kG, and $(BH)_{max}$ = 7.5 MGOe was produced when LPBF was performed under the conditions of P90, V500, H70, and L30 (volume energy density = 85.7 J/mm^3). The solidification behavior of Nd-Fe-B magnets during LPBF was analyzed in detail using thermodynamic simulations. In this study, the microstructure of the fusion zone (FZ) and the heat affected zone (HAZ) according to process parameters was analyzed, and the effect of the solidification microstructure on the magnetic properties of Nd-Fe-B magnets was reported.

1. Introduction

Permanent magnets have become essential components in various industries, including automotive, electronics, and renewable energy [1]. Since their development in the 1980s, Nd-Fe-B magnets have exhibited excellent performance in terms of maximum energy product $(BH)_{max}$, remanence, and coercivity, outperforming all other existing permanent magnet varieties [2]. Currently, nanocrystalline Nd-Fe-B magnets are manufactured using melt-spinning technology, which enables the creation of very fine grains or nanocrystals, as well as amorphous materials. However, the thickness of the ribbon produced is limited to ensure a rapid cooling rate. Unlike the typical rapid cooling technique, the additive manufacturing (AM) process has no restrictions on the part thickness owing to its layer-by-layer production characteristics. AM has emerged as a sustainable approach to producing near-net-shaped permanent magnets with complex geometries. The cooling rate of the melt pool used in the laser powder bed fusion (LPBF) process ranges from 10^5 to 10^7 K/s, significantly higher than other additive manufacturing processes [3]. LPBF uses a laser to melt thin layers of spherical powder [4]. After each layer solidifies, a fresh layer of powder is provided, and the process is repeated until the final three-dimensional objects are fabricated. LPBF offers the advantage of producing magnets with a refined microstructure, which is beneficial for magnetic properties regardless of the size or shape of the part. Ja'cimovi'c et al. [5] reported that the B_r and $(BH)_{max}$ values of LPBF magnets are significantly higher than those of injection-molded or SPS-sintered magnets.

Most studies on the LPBF process for fabricating permanent magnets have focused on the effect of the process parameters on the magnetic properties of Nd-Fe-B-based magnets. Bittner et al. [6] compared the magnetic properties of Nd-Fe-B magnets fabricated via LPBF at various area energy densities (E_A = P/VH) and observed the melt pool to investigate the relationship between the microstructure and magnetic

* Corresponding authors.
E-mail addresses: adream@kitech.re.kr (D.-R. Eo), wooyoung@yonsei.ac.kr (W. Lee).

https://doi.org/10.1016/j.matchar.2024.114228
Received 12 March 2024; Received in revised form 18 July 2024; Accepted 28 July 2024
Available online 30 July 2024

properties. The magnetic properties improved as the area energy density increased within the range of E_A = 0.5–2.4 J/mm^2. Bittner et al. [7] reported that the coercivity increased linearly as the line energy density increased—that is, the magnetic properties and density of the LPBF magnet increased as the laser power increased and the scan speed or hatch distance decreased. If the volume energy density was too low, the LPBF magnet exhibited soft magnet behavior with very low coercivity, and the magnetic properties improved as the volume energy density (VED) increased in the range of E_v = 18–79 J/mm^3 [8]. Kolbet et al. [9] reported that a low line energy and high hatch distance resulted in low density and brittleness of the LPBF sample, owing to insufficient energy for complete remelting of the powder. When other parameters were the same, the samples with a small hatch distance had a higher density than those with a large hatch distance. Skalon et al. [10] compared the magnetic properties based on layer thickness. The magnetic properties increased as the layer thickness decreased in the range of 40–120 μm. Other studies have investigated the effects of adding materials to improve the magnetic properties of LPBF magnets. Huberet et al. [11] demonstrated that the coercivity of LPBF Nd-Fe-B magnets could be increased by grain boundary diffusion (GBD) treatment with a low-melting-point rare-earth eutectic alloy. Jianet et al. [12] confirmed that magnetic properties improved after the addition of other spherical powders.

However, it is difficult to find a study that specifies the phase transformation behavior during the LPBF process, that is, how the microstructure and phase change and redistribute during remelting and rapid cooling in the LPBF process. Therefore, in this study, the microstructure and phase changes that occur during solidification under various volume energy densities in the LPBF process and the effects of these changes on the magnetic properties were studied in detail.

2. Experimental procedures

2.1. Materials

Cylindrical samples of Φ10 × L6 (mm) (Fig. 1) were fabricated using commercially available spherical Nd-Fe-B powder (MQP-S-11-9-20,001) with a particle size range of 18 to 43 μm. The composition of the powder consisting of the (Nd, Pr)$_2$Fe$_{14}$B/ α-Fe nanocomposite structure was $Nd_{7.5}Pr_{0.7}Zr_{2.6}Ti_{2.5}Co_{2.5}Fe_{75.4}B_{8.8}$. Bulk Nd-Fe-B magnets were manufactured on 316 L stainless steel plate, using an LPBF machine (Metalsys 250, Winforsys, South Korea) equipped with an IPG YLR-400-AC fiber laser with a spot size of about 100 μm. The LPBF process was performed in an Ar atmosphere to prevent oxidation during the process. The process chamber was filled with Ar gas, and the oxygen content was maintained at 10.7 ppm using a zirconia oxygen analyzer (Daiichi Nekken, Japan). Throughout the LPBF process, fresh Ar gas was supplied constantly to the chamber.

Four different process conditions were adopted to produce magnetic samples with similar densities under each condition (Table 1). The layer thickness was fixed at 30 μm. To reduce residual stress and cracks, it was fabricated by applying a rotation of 67° [13]. The relative densities of the samples were measured using Archimedes' method. The theoretical density of the alloy was 7.43 g/cm^3 [14]. The volume energy density (VED, E_v) was calculated using the well-known equation E_v = P/vht (where P is the laser power, v is the scan speed, h is the hatch thickness, and t is the layer thickness) [15].

2.2. Characterizations

The demagnetization curves of the as-built magnets were measured using a B—H hysteresis loop tracer (Permagraph C-300, Magnet-Physik). X-ray diffraction (XRD; Bruker, D8 Advance) using Cu Kα radiation (40 kV, 30 mA) was performed to analyze the phases. A section of the as-built magnet was cut along the building direction and polished using conventional metallurgical techniques. The microstructure was observed using scanning electron microscopy (SEM, JSM-7610F-Plus, Jeol) in the backscattered electron mode (BSE). Transmission electron microscopy (TEM) was performed using a JEM-ARM 200F NEOARM instrument equipped with a Cs corrector capable of correcting spherical aberrations. Energy-dispersive X-ray spectroscopy (EDS) was performed using a dual SDD EDS system.

3. Results

3.1. The magnetic properties

The magnetic properties of LPBF Nd-Fe-B magnets with different

Table 1
LPBF process parameters for Nd-Fe-B bulk magnet samples.

Label	Laser Power [W]	Scan Speed [mm/s]	Hatch Distance [μm]	Volumetric energy Density [J/mm^3]	Relative density [%]
E_v–83	90	900	40	83.3	88.8
E_v–85	90	500	70	85.7	90.2
E_v–166	60	300	40	166.7	87.6
E_v–222	40	150	40	222.2	80.0

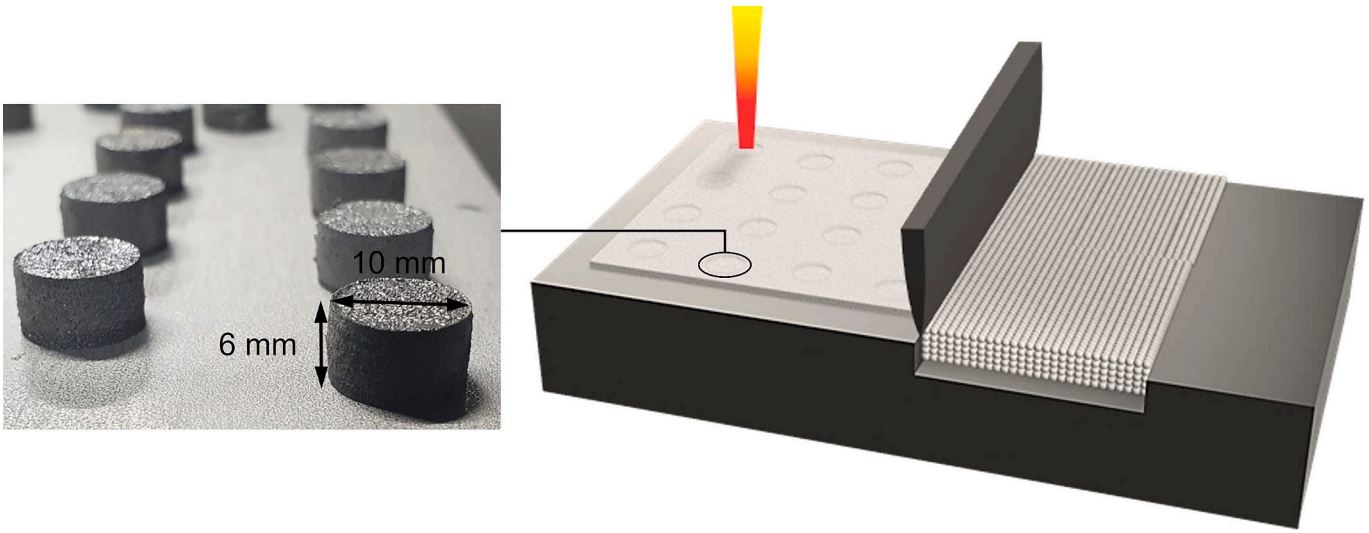

Fig. 1. Photographs of the as-built Nd-Fe-B magnet specimens.

volume energy densities are shown in Fig. 2.

Fig. 2(a) shows the demagnetization curves of the initial powder and LPBF magnets. The initial powder, consisting of 2:14:1/α-Fe nanocomposites, exhibits a demagnetization curve typical of an isotropic magnet due to exchange coupling between hard and soft magnetic phases. However, the magnets made with high energy density (E_v-166, E_v-222) exhibit demagnetization curves that appear when exchange coupling does not occur or when coarse nanograins of soft and hard magnetic phases are mixed (i.e., rapid reduction in magnetization in the low-demagnetizing-field region), which suggests that coarse soft magnetic α-Fe was crystallized during the LPBF process. The change in the demagnetization curve was attributed to the change in the cooling rate caused by the change in the volume energy density rather than the change in the relative density. When the volume energy density was low (E_v-83, E_v-85), the change in the demagnetization curve was gradual, which suggests that the crystallization of soft magnetic α-Fe was suppressed owing to the rapid cooling rate and therefore did not affect the shape of the demagnetization curve.

In general, the remanence (B_r) of an isotropic magnet is proportional to its density and the amount of ferromagnetic phase in the magnet. Fig. 2(b) shows the change in the B_r values of the magnets fabricated using LPBF as a function of the relative density. As the relative density increases, the B_r values increase proportionally. Therefore, the magnet fabricated by LPBF at E_v-85 with the highest relative density (90.2%) exhibited the highest B_r value of 6.2 kG (Table 1). However, a sufficiently high density of more than 95% was never obtained, which is closely related to numerous pores and cracks in all samples. Therefore, to maximize B_r and $(BH)_{max}$, it is essential to establish process parameters that can improve the density of the sample by minimizing the defects that occur in the LPBF process. As shown in Fig. 2(a), the best magnetic properties were obtained from the magnet fabricated by LPBF with E_v-85, with B_r = 6.2 kG, H_{ci} = 10.3 kOe, and $(BH)_{max}$ = 7.5 MGOe. These magnetic properties were superior to those of the bonded magnets manufactured using the initial powder [16].

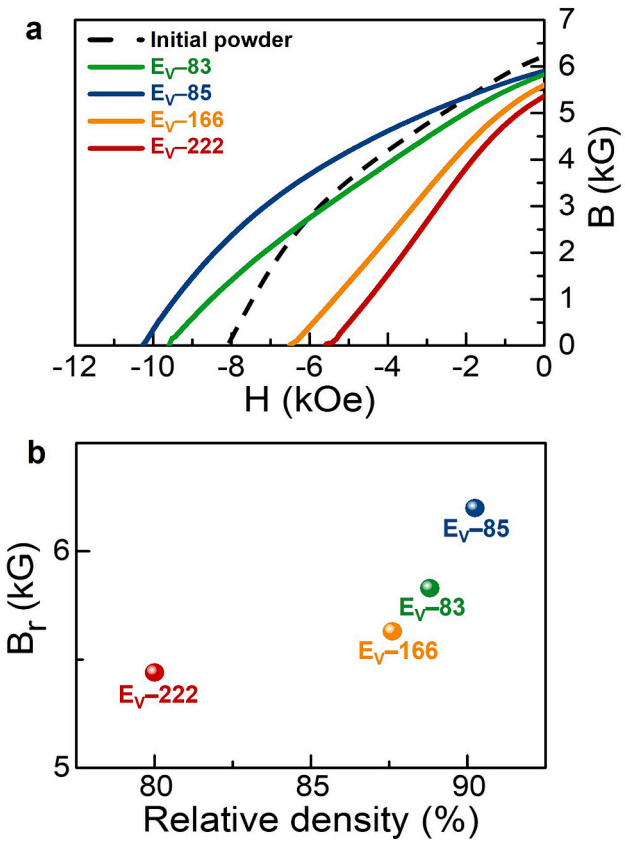

Fig. 2. (a) Demagnetization curves of as-received Nd-Fe-B powder and LPBF Nd-Fe-B bulk magnets. (b) Variation of remanence value with respect to the relative density of LPBF Nd-Fe-B bulk magnets.

In comparison with the results of other studies that used the same powder used in this study, we found that similar magnetic properties can be obtained if the samples are fabricated with similar volume energy densities (E_v). When the sample was fabricated with an E_v similar to that of our sample with a slow cooling rate (E_v-166), i.e., with $E_v \sim 153$ J/mm^3 (P/V = 0.429 J/mm, L 15 μm, H 140 μm, and the relative density 94%) [17], magnetic properties of B_r = 5.2 kG, H_{cj} = 6.5 kOe, and $(BH)_{max}$ = 4.2 MGOe were obtained. However, when the sample was fabricated with $E_v \sim 63$ J/mm^3 (P/V = 0.067 J/mm, L 30 μm, H 35 μm, and the relative density 85%) [7], similar to our sample (E_v-83 and E_v-85) with a fast cooling rate, magnetic properties of B_r = 6.3 kG, H_{ci} = 11.1 kOe, and $(BH)_{max}$ = 7.9 MGOe were obtained. This indicates that even if LPBF is performed in different environments, similar magnetic properties are obtained if the volume energy density is similar, which indicates that the volume energy density is the most important parameter for the LPBF process.

To investigate the effects of the microstructural and phase changes that occur during LPBF on the changes in magnetic properties, a systematic analysis of the phases and microstructures was performed using XRD, SEM, and TEM.

Fig. 3 shows the powder XRD patterns of the initial powder and LPBF-processed bulk magnets. The main phase in both the initial powder and LPBF magnets was $(Nd, Pr)_2Fe_{14}B$ (2:14:1). The broad peak patterns indicated that both powders were composed of very fine grains. The α-Fe peak is detected in the initial powder possessing a nanocomposite structure of 2:14:1/ α-Fe, but the peak is not observed in the LPBF-processed magnets, implying that phase and microstructural changes occurred during LPBF. According to TEM observation [11], as expected, the initial powder had a microstructure consisting of 2:14:1 and α-Fe with a size of 20–30 nm. In the latter part of the study, a comprehensive phase analysis of the LPBF-processed magnet was conducted using a TEM diffraction pattern analysis.

3.2. Microstructure

Fig. 4 shows a cross-sectional view of the LPBF sample in the build direction. Regardless of the VED (volume energy density), the samples produced by the LPBF process were all composed of fusion zone (FZ) and

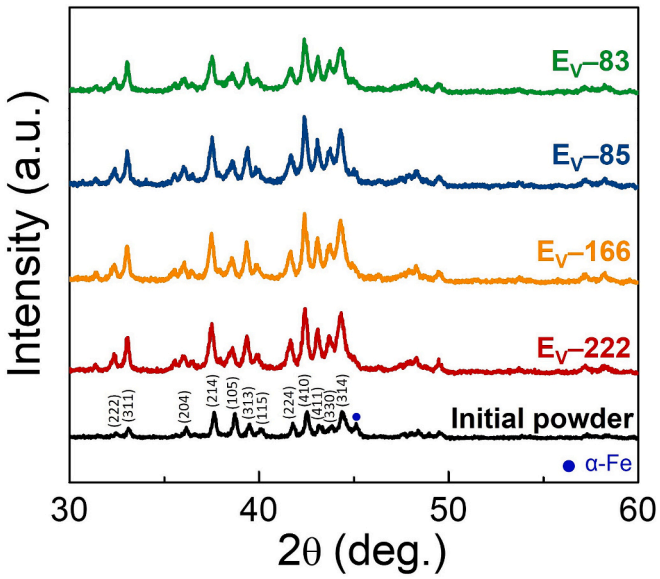

Fig. 3. Powder XRD pattern of as-received Nd-Fe-B powder and LPBF-processed Nd-Fe-B bulk magnets.

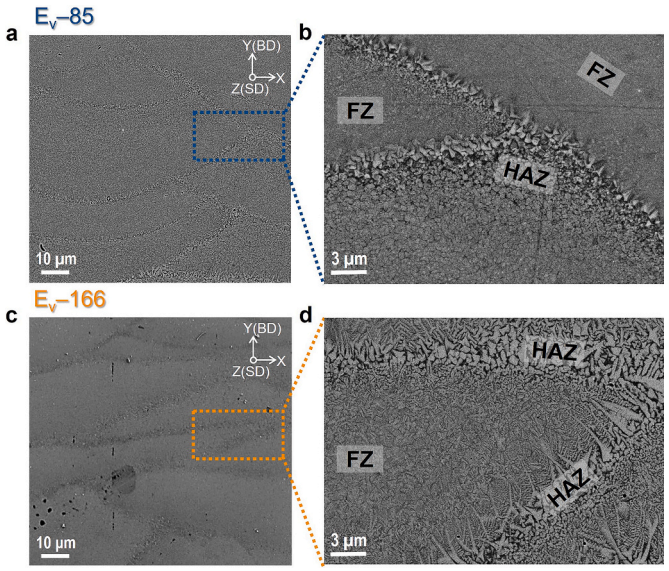

Fig. 4. SEM-BSE cross-sectional view of LPBF samples along the build direction for E_v–85 (a, b) and E_v–166 (c, d). Enlarged portions of HAZ are shown in (b) and (d).

heat affected zone (HAZ). However, the proportion of each variable varied depending on VED. In the samples with a small VED, i.e., with a fast-cooling rate, the proportion of HAZ was approximately 10%, which was less than that in the samples with a slow cooling rate. In the samples with a large VED due to a slow cooling rate, the HAZ was observed to be approximately 20%, and the FZ was approximately 80%. A HAZ with relatively large particles was found along the melt pool boundary.

Fig. 5 shows the differences in the grain size and morphology between the FZ and HAZ depending on the VED. In the E_v-85 sample, the grains in the FZ were too fine (less than 100 nm) to distinguish the grain structure using SEM, and some were shown to be amorphous regions

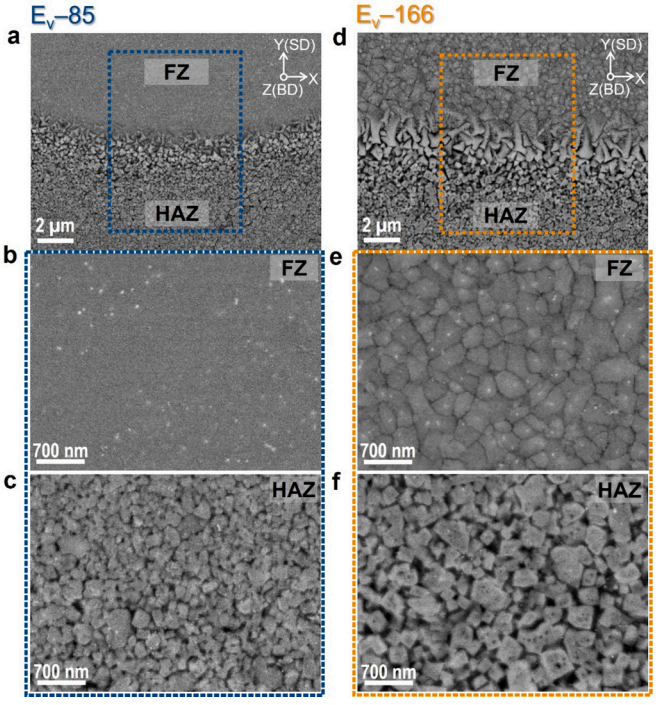

Fig. 5. SEM-BSE cross-sectional views of LPBF samples normal to the build direction for E_v-85 (a–c) and E_v-166 (d–f).

formed by rapid cooling. By contrast, relatively large particles (300–500 nm) are observed in the FZ of E_v-166. In the HAZ region, the shape of the 2:14:1 grains changed to a cubic shape owing to the instantaneous temperature rise, regardless of the VED. Simultaneously, the 2:14:1 grains grew significantly in E_v-85. Also, in E_v–166, epitaxial growth of columnar dendrite from the partially-melted grains on the melt pool boundary was noticeable, while, in E_v–85, the epitaxial growth of the partially-melted grains was also under-developed. (Fig. 5(a) and (d)).

Fig. 6 shows the microstructure and elemental analysis results of the FZ and HAZ of the E_v-85 sample observed using TEM. As shown in Fig. 6 (a), large and small equiaxed 2:14:1 grains of nanometer size (less than 300 nm) were surrounded by black grain boundary phases in the FZ. These black grain boundary phases are Ti-rich amorphous phases within a few nanometers, as shown in Fig. 6(b) and (a-6). In the HAZ, which experienced additional thermal cycle, the 2:14:1 grains developed more clearly and turned into a cubic shape, as shown in Fig. 6(d), and the amorphous grain boundary phase was also much thicker. In addition, Zr, which was uniformly dispersed in the FZ, was concentrated at the grain boundaries, resulting in the grain boundary phase becoming a (Ti, Zr)-rich phase. The reason Zr is more distinctly visible in the HAZ is due to the repulsion or redistribution of elements like Zr during these instantaneous thermal cycles, as such is thermodynamically more stable.

Interestingly, Nd-rich droplets were mostly found within the 2:14:1 grains near the grain boundaries of the FZ and HAZ. These were considered Nd oxides formed during the LPBF process, which was engulfed during the rapid solidification of 2:14:1 grains and remained in the grain. Consequently, the 2:14:1 grains in the FZ and HAZ of the Ev-85 sample are all surrounded by grain boundary phases regardless of the grain size, indicating that the 2:14:1/ α-Fe nanocomposite structure of the initial powder was no longer maintained after LPBF.

A microstructural morphology in which hard magnetic 2:14:1 grains are separated by a grain boundary phase is commonly found in Nd-Fe-B sintered magnets or melt-spun alloys. In addition, it was confirmed that **α**-Fe does not crystallize not only in the FZ but also in the HAZ owing to the sufficiently fast cooling rate. That is, as shown in the Fe distribution in Figs. 6(a-2) and (d-2), all the Fe that did not participate in the formation of 2:14:1 appeared to have been amorphized along the grain boundaries. The higher coercivity of the **E_v**-85 magnet than the initial powder in Fig. 2 is because the magnetic coupling between the hard magnetic 2:14:1 grains is weakened by the separation of the grains with the amorphous grain boundary phase. If the grain boundary phases were not soft magnetic but nonmagnetic, the magnetic decoupling between the 2:14:1 grains would have been enhanced, further increasing coercivity [18].

Fig. 7 shows the microstructure and elemental distribution in the FZ and HAZ of the E_v-166. As shown in Fig. 7(a), the 2:14:1 grains and grain boundary phases in the FZ were larger and thicker than those in E_v-85. This type of microstructure, in which equiaxed 2:14:1 grains of several hundred nanometers in size are well separated by grain boundary phases and distributed uniformly, is also clearly shown in Fig. 5(e). As shown in Figs. 7(a-2) and (b), the grain boundary phase in the E_v-166 sample was basically amorphous, although approximately 100 nm α-Fe precipitated along the grain boundaries. In addition, the grain boundary phase, excluding α-Fe, was (Ti, Zr)-rich, as found in the HAZ of E_v-85 (see Figs. 7(a-4) and (a-6)).

The phase distribution in the HAZ, which was momentarily subjected to a temperature rise, was identical to that in the FZ. However, the overall microstructure became coarser. In particular, the (Ti, Zr)-rich grain boundary phase developed more prominently, and the 2:14:1 grains at HAZ experienced instantaneous temperature rise, and the shape of the grains transformed into angular shapes (see Fig. 5(f)). The reason is to expose a specific habit plane that can reduce interfacial energy to the surface, in order to lower the interfacial energy. It is assumed that the exposure of the 110 plane on the surface as seen in Fig. 6e is due to this context. The size of α-Fe crystallized along the grain boundary phase also increased, often exhibiting α-Fe particles as large as

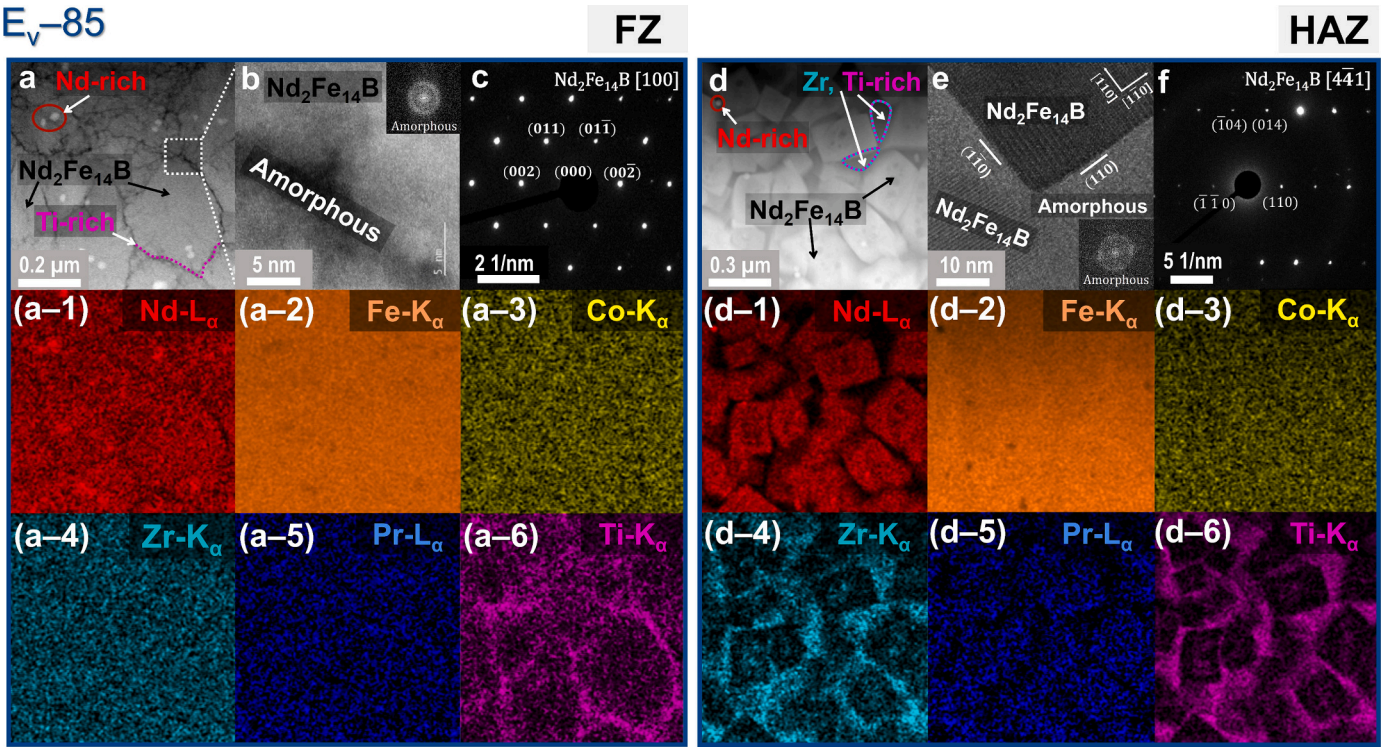

Fig. 6. TEM results for an LPBF magnet at E_v-85: (a) HAADF-STEM image of FZ. (b) High-resolution HAADF-STEM image revealing an amorphous grain boundary phase. The corresponding fast Fourier transformation (FFT) pattern is shown in the upper right-hand corner. (c) Selected-area electron diffraction (SAED) pattern of a $Nd_2Fe_{14}B$ grain in zone axis [100]. STEM-EDS element mapping results of (a) are shown in (a-1) to (a-6). (d) HAADF-STEM image of HAZ. (e) High-resolution HAADF-STEM image revealing an amorphous phase between tetragonal $Nd_2Fe_{14}B$ grains. The corresponding fast Fourier transformation (FFT) pattern is shown in the lower right-hand corner. (f) SAED pattern of a $Nd_2Fe_{14}B$ grain in zone axis [4$\bar{4}$1]. STEM-EDS element mapping results of (d) are shown in (d-1) to (d-6).

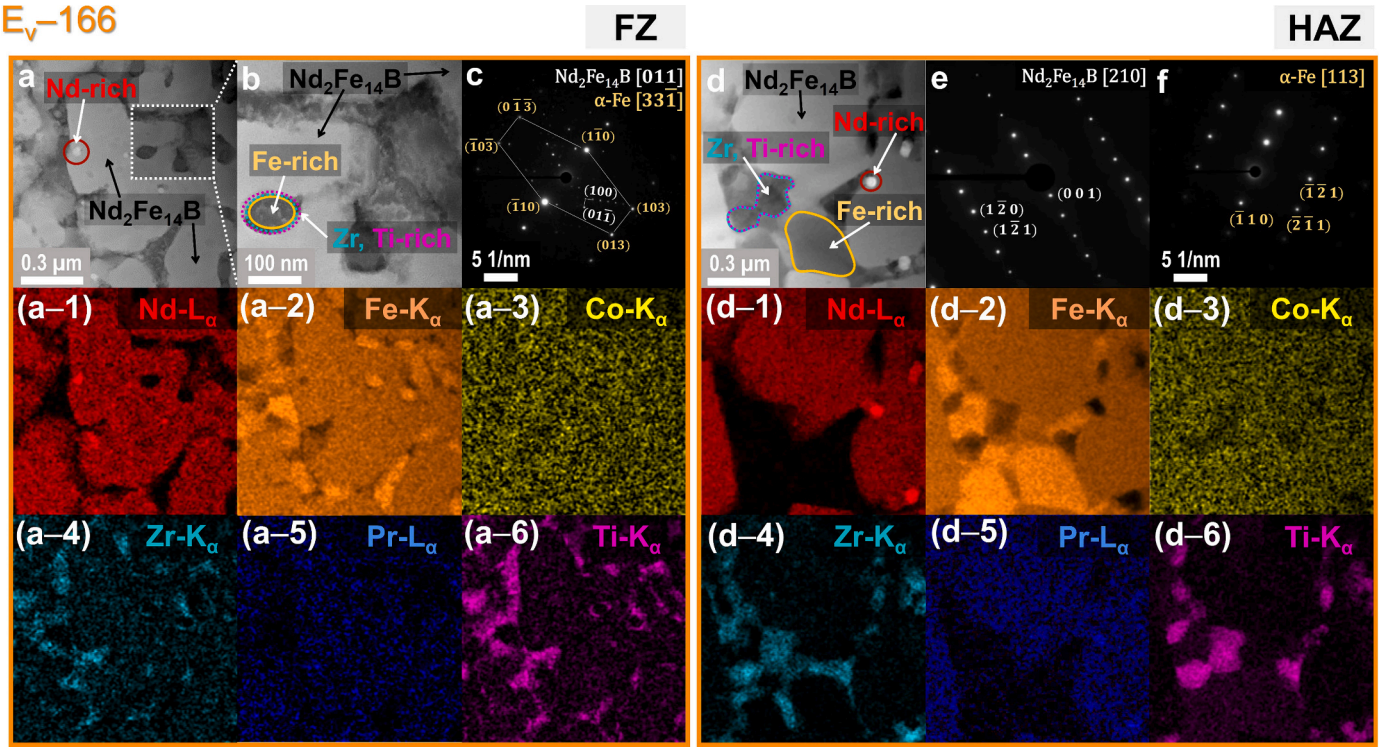

Fig. 7. TEM results for an LPBF magnet at E_v-166: (a) HAADF-STEM image of FZ. (b) High-resolution HAADF-STEM image revealing α-Fe crystalized in amorphous grain boundary phase. (c) SAED patterns of a $Nd_2Fe_{14}B$ grain in the zone axis of [011] and α-Fe in the zone axis of [33$\bar{1}$]. (a-1) to (a-6) STEM-EDS element mapping results of (a). (d) HAADF-STEM image of HAZ. (e) and (f) SAED patterns of a $Nd_2Fe_{14}B$ grain in the zone axis of [210] and α-Fe in the zone axis of [113], respectively. STEM-EDS element mapping results of (d) are shown in (d-1) to (d-6).

300 nm (see Figs. 7(d) and (d-2)).

In addition, Nd-rich droplets larger than those found in the E_v-85 sample were observed near or within the grain boundaries of the 2:14:1. This indicates that the Nd-oxide in E_v-85 does not have time to migrate to the grain boundaries because of the rapid solidification rate but rather remains in the grains, whereas in E_v-166, it migrates to the grain boundaries and is distributed there as the cooling rate decreases. Composition analysis revealed that the amorphous (Ti, Zr)-rich grain-boundary phase contained a significant amount of boron. This suggests that the boron remaining after the formation of the 2:14:1 phase accumulated at the grain boundaries and promoted the amorphization of the grain boundary phase.

Consequently, α-Fe crystallizes along the grain boundaries in both the FZ and HAZ in the E_v-166 sample, and the 2:14:1 grains, regardless of their size and shape, are separated by amorphous (Ti, Zr)-rich grain boundary phases and soft magnetic α-Fe. The presence of such α-Fe in the E_v-166 sample is responsible for the lower coercivity than the initial powder and the rapid decrease in residual magnetization in the low demagnetizing field region, as shown in Fig. 2(a).

4. Discussion

To determine the phase changes that occur during the remelting and solidification processes in LPBF, we examined the phase relationship of the alloy composition used in this study. Fig. 8 (a) shows the vertical section (Fe:B = 14:1) of the Nd-Fe-B phase diagram [19,20], and Fig. 8 (b) shows a schematic of the continuous cooling curve of the Nd-Fe-B alloy used in this study (composition indicated by the orange dotted line in Fig. 8 (a)) during rapid solidification. Since the rare earth (Nd and Pr) content of the powder used in this study is 8.2 at.% when solidification occurs under normal conditions, γ-Fe first crystallizes from the liquid phase along the orange dotted line shown in Fig. 8(a) (A), and then as the temperature drops below point B, $Nd_2Fe_{14}B$ (T_1 phase) crystallizes by the peritectic reaction (L + γ-Fe ➔ $Nd_2Fe_{14}B$). As the temperature drops further, γ-Fe finally transforms to α-Fe, resulting in the microstructure of α-Fe + $Nd_2Fe_{14}B$ at room temperature. However, as reported by Branagan et al. [19], rapid cooling prevents the nucleation and growth of γ-Fe in the liquid phase, leading to the crystallization of $Nd_2Fe_{14}B$ through eutectic-like reactions. As shown in Fig. 8(b), when the cooling rate is sufficiently high (E_v-85), only $Nd_2Fe_{14}B$ crystallizes, and Fe crystallization is suppressed until the supercooled liquid reaches the glass transition temperature (T_g). Consequently, the residual liquid containing Fe becomes entirely amorphous below the glass transition temperature (T_g), forming an amorphous grain boundary phase, as observed in the E_v-85 sample (see Fig. 6). However, if the cooling rate slows down due to an increase in energy density (as in the case of E_v-166) [21], the crystallization of α-Fe also occurs in addition to $Nd_2Fe_{14}B$, and the residual liquid that has not solidified until Tg becomes amorphous. Eventually, when the solidification process is completed, the final microstructure is formed in such a way that $Nd_2Fe_{14}B$ matrix grains are surrounded by an amorphous grain boundary phase and a secondary α-Fe crystallized at the grain boundaries, as shown in Fig. 7.

Meanwhile, as the solidification of $Nd_2Fe_{14}B$ progressed, the Nd content in the liquid phase decreased, and the Zr and Ti contents in the residual liquid phase increased owing to the solubility limits of Zr and Ti in the $Nd_2Fe_{14}B$ phase. Considering the composition of the initial powder with a relatively high amount of B, the B remaining after participating in the formation of the $Nd_2Fe_{14}B$ phase also resides in the liquid phase. This B, which is a typical vitrification element, will delay the solidification of α-Fe [22] and promote the amorphization of the residual liquid phase.

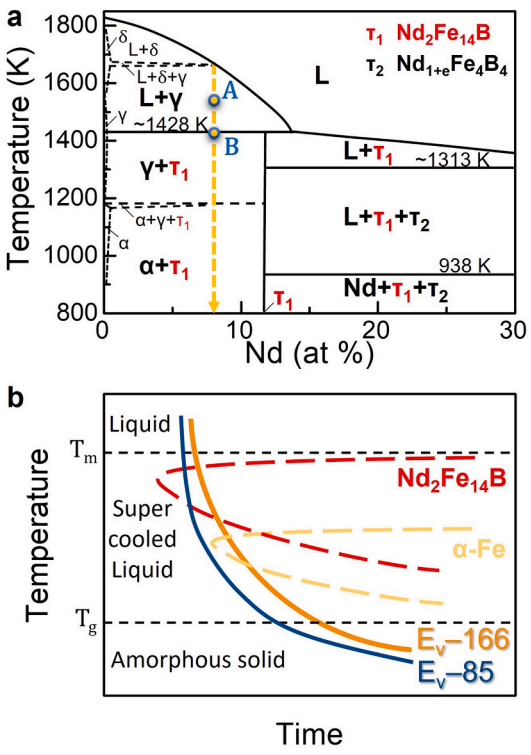

Fig. 8. (a) Vertical section of the Nd-Fe-B phase diagram. (b) Schematic continuous cooling transformation (CCT) diagram of Nd-lean Nd-Fe-B shown with a dotted line in (a).

Fig. 9 shows the thermodynamic simulation results of the solute concentration change in the liquid phase during the solidification process obtained using the commercial software FactSage. Because the Pr and Co components in the initial powder can be substituted for Nd and Fe in $Nd_2Fe_{14}B$, respectively, the Pr content in the initial powder composition was combined with the Nd content, and the Co content was combined with the Fe content for the calculation. If supercooling is not considered, the solidification of the liquid phase begins at 1125 °C and ends near 900 °C, where all the Nd in the liquid phase is consumed by the crystallization of $Nd_2Fe_{14}B$ (Fig. 9(a)). As solidification proceeded, the concentrations of B, Zr, and Ti in the residual liquid increased, whereas the concentration of Fe decreased. Eventually, the residual liquid solidified into an amorphous state (Fig. 9(b)). In particular, the increase in the B content in the liquid phase significantly contributes to the amorphization of the residual liquid. Thus, the amorphized residual liquid forms a grain boundary phase and affects the magnetic interaction between the ferromagnetic crystalline grains. Therefore, the chemical composition and magnetic properties of the residual liquid are important factors that determine the magnetic properties, especially the coercivity, of Nd–Fe–B magnets manufactured using LPBF. As shown in the simulation results of Fig. 9(b), all the samples manufactured by LPBF in this study appear to have a ferromagnetic grain boundary phase. This is because the Fe content is high in the grain boundary phase of the E_v-85 sample, in which α-Fe did not crystallize but was completely amorphous, as well as in the E_v-166 sample, in which α-Fe crystallized at the grain boundary owing to the relatively slow cooling rate. When a ferromagnetic grain boundary phase is formed in this manner, the magnetic decoupling between the hard magnetic 2:14:1 grains is weakened, making it difficult to expect a large coercivity. This also explains why the

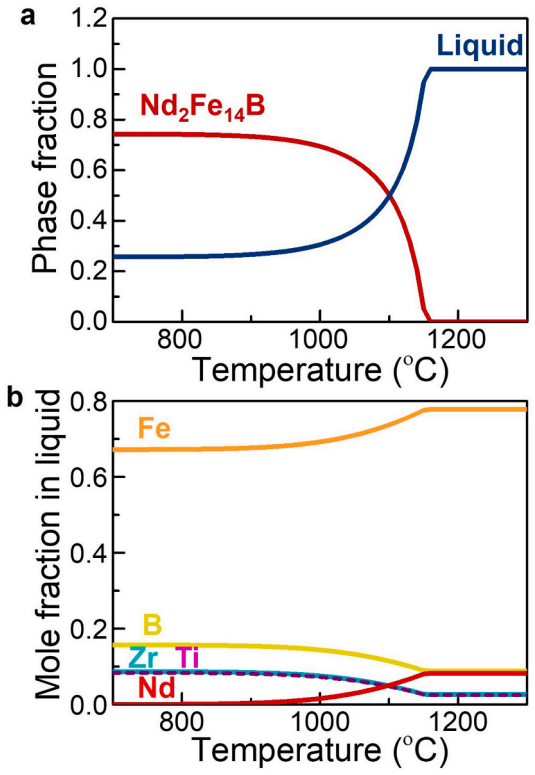

Fig. 9. Simplified thermodynamic simulation for the solidification process of $Nd_2Fe_{14}B$ in the melt pool: (a) Variation of phase fraction during the solidification, (b) Variation of solute concentration in the liquid phase.

increase in the coercivity of the E_v-85 sample was limited. In the case of the E_v-166 sample, where α-Fe precipitated at the grain boundary due to the relatively slow cooling rate, magnetic coupling actually occurred between the hard magnetic grains because of this α-Fe, resulting in a significant decrease in coercivity (see Fig. 2(a)).

Considering the composition of the initial powder used in this study, which has less Nd but higher Fe than the stoichiometric composition of $Nd_2Fe_{14}B$, it is inevitable that a grain boundary phase with a high Fe content is formed after the formation of $Nd_2Fe_{14}B$ during the remelting and solidification process in the LPBF. Therefore, as demonstrated by Goll et al. [23], by modifying the alloy design to reduce the Fe content in the grain boundary phase and increase the content of nonmagnetic elements such as Nd, it would be possible to form a nonmagnetic grain boundary phase. This can enhance the magnetic decoupling effect between the hard magnetic grains, producing magnets with higher coercivity. Therefore, when the magnetic properties are concerned, it is not desirable to use an Nd-lean Nd-Fe-B powder, such as that used in this study, in the LPBF process, where full remelting occurs. Instead, it is desirable to select spherical alloy powders with a composition that contains at least more Nd than $Nd_2Fe_{14}B$ and is close to the stoichiometric composition of $Nd_2Fe_{14}B$.

5. Conclusions

When LPBF was performed with the spherical powder of Nd-lean Nd-Fe-B alloy, the 2:14:1/α-Fe nanocomposite structure of the initial powder was no longer maintained in the LPBF samples, and their microstructure changed to a new form after undergoing the complete remelting and solidification process. This new microstructure, in which nanoscale 2:14:1 grains were separated by an amorphous grain boundary phase, was obtained when the cooling rate was sufficiently fast, that is, when the VED was relatively low, as in the case of E_v-85. This structural arrangement is beneficial for improving the coercivity of the LPBF magnets.

However, the increase in coercivity was limited because of the formation of a soft magnetic amorphous grain boundary phase owing to the high Fe content in the grain boundary phase originating from the powder composition. Therefore, by adjusting the powder composition to form an amorphous grain boundary phase with less Fe, the grain boundary phase can be changed to a nonmagnetic phase, which improves the magnetic decoupling effect between the hard magnetic grains, resulting in higher coercivity. In any case, the cooling rate should be maintained sufficiently fast to prevent the crystallization of α-Fe during the LPBF process. Another problem that needs to be solved is how to maximize the remanence by increasing the density of a sample and minimizing the occurrence of defects associated with LPBF.

Based on the results of this study, the following modifications are required to manufacture magnets with superior magnetic properties using LPBF. First, the alloy design should be optimized to obtain a spherical initial powder with a composition that has a higher Nd content than stoichiometric $Nd_2Fe_{14}B$ to facilitate the formation of a nonmagnetic grain boundary phase while maximizing the volume fraction of the hard magnetic phase for high magnetization values. Second, process conditions should be established to minimize the occurrence of defects, such as pores and cracks, during LPBF, thereby maximizing the density of the magnet. By optimizing the alloy design and LPBF process conditions, it is possible to produce samples with a high volume fraction of the hard magnetic phase, high density, and nonmagnetic grain boundary phases. This would lead to near-*net*-shaped isotropic magnets possessing advanced magnetic properties compared to polymer-bonded commercial magnets. The results of this study provide a valuable starting point for such modifications.

CRediT authorship contribution statement

Ho-Jeong Kim: Writing – review & editing, Writing – original draft, Visualization, Methodology, Investigation, Data curation. **Ye Ryeong Jang:** Validation. **Hyun-Sook Lee:** Visualization. **Jung-Wook Cho:** Resources. **Taesuk Jang:** Writing – review & editing, Validation. **Du-Rim Eo:** Writing – original draft, Resources, Methodology, Investigation, Conceptualization. **Wooyoung Lee:** Supervision, Resources, Funding acquisition.

Declaration of competing interest

The authors declare that they have no known competing financial interests or personal relationships that could have appeared to influence the work reported in this paper.

Data availability

Data will be made available on request.

Acknowledgement

This work was supported by the Technology Innovation Program (“20013621,” Center for Super Critical Material Industrial Technology) funded by the Ministry of Trade, Industry & Energy (MOTIE, Korea), the National Research Foundation of Korea (NRF) and a grant from the Commercialization Promotion Agency for R&D Outcomes (COMPA) funded by the Korean Government (MSIT) (RS-2023-00238493), and the Basic Science Research Program through the National Research Foundation of Korea (NRF) (NRF-2019R1A6A1A11055660). This work was also supported by the Korea Institute of Industrial Technology as an internal project (UR230019).

References

[1] L. Li, K. Jones, B. Sales, J.L. Pries, I.C. Nlebedim, K. Jin, H. Bei, B.K. Post, M. S. Kesler, O. Rios, V. Kunc, R. Fredette, J. Ormerod, A. Williams, T.A. Lograsso, M. P. Paranthaman, Fabrication of highly dense isotropic Nd-Fe-B nylon bonded magnets via extrusion-based additive manufacturing, Addit. Manuf. 21 (2018) 495–500.

[2] M. Sagawa, S. Fujimura, N. Togawa, H. Yamamoto, Y. Matsuura, New material for permanent magnets on a base of Nd and Fe, J. Appl. Phys. 55 (1984) 2083–2087.

[3] P.A. Hooper, Melt pool temperature and cooling rates in laser powder bed fusion, Addit. Manuf. 22 (2018) 548–559.

[4] H. Attar, K.G. Prashanth, L.-C. Zhang, M. Calin, I.V. Okulov, S. Scudino, C. Yang, J. Eckert, Effect of powder particle shape on the properties of in situ Ti–TiB composite materials produced by selective laser melting, J. Mater. Sci. Technol. 31 (2015).

[5] J. Jacimovic, F. Binda, L.G. Herrmann, F. Greuter, J. Genta, M. Calvo, T. Tomse, R. A. Simon, Net Shape 3D Printed NdFeB Permanent Magnet, ArXiv Prepr. ArXiv1611.05332, 2016.

[6] F. Bittner, J. Thielsch, W.-G. Drossel, Microstructure and magnetic properties of Nd-Fe-B permanent magnets produced by laser powder bed fusion, Scr. Mater. 201 (2021) 113921.

[7] F. Bittner, J. Thielsch, W.-G. Drossel, Laser powder bed fusion of Nd–Fe–B permanent magnets, Prog. Addit. Manuf. 5 (2020) 3–9.

[8] F. Bittner, J. Thielsch, W.-G. Drossel, Unexpected coercivity enhancement> 1T for Nd-Fe-B permanent magnets with 20 wt% Nd produced by laser powder bed fusion, IEEE Trans. Magn. 58 (2022) 1–5.

[9] T. Kolb, F. Huber, B. Akbulut, C. Donocik, N. Urban, D. Maurer, J. Franke, Laser beam melting of ndfeb for the production of rare-earth magnets, in: 2016 6th Int. Electr. Drives Prod. Conf, IEEE, 2016, pp. 34–40.

[10] M. Skalon, M. Görtler, B. Meier, S. Arneitz, N. Urban, S. Mitsche, C. Huber, J. Franke, C. Sommitsch, Influence of melt-pool stability in 3D printing of NdFeB magnets on density and magnetic properties, Materials (Basel) 13 (2019) 139.

[11] C. Huber, H. Sepehri-Amin, M. Goertler, M. Groenefeld, I. Teliban, K. Hono, D. Suess, Coercivity enhancement of selective laser sintered NdFeB magnets by grain boundary infiltration, Acta Mater. 172 (2019) 66–71.

[12] W.Y.J. Jian, C.W. Cheng, W.C. Chang, T.Y. Huang, Y.C. Liang, A.C. Lee, T. W. Chang, M.C. Tsai, Fabrication of crack-free Nd-Fe-B magnets with laser powder bed fusion, Materialia 21 (2022) 101351.

[13] A. Paraschiv, G. Matache, N. Constantin, M. Vladut, Investigation of scanning strategies and laser remelting effects on top surface deformation of additively manufactured IN 625, Materials 15 (2022) 3198.

[14] J.F. Herbst, R 2 Fe 14 B materials: intrinsic properties and technological aspects, Rev. Mod. Phys. 63 (1991) 819.

[15] T. DebRoy, H.L. Wei, J.S. Zuback, T. Mukherjee, J.W. Elmer, J.O. Milewski, A. M. Beese, A.D. Wilson-Heid, A. De, W. Zhang, Additive manufacturing of metallic components—process, structure and properties, Prog. Mater. Sci. 92 (2018) 112–224.

[16] Neo Magnequench: MQP-S-11-9-20001-070 Powder Datasheet, 2024.

[17] K.S. Yu, C.W. Cheng, A.C. Lee, W.Y.J. Jian, W.C. Chang, T.W. Chang, M.C. Tsai, Additive manufacturing of NdFeB magnets by synchronized three-beam laser powder bed fusion, Opt. Laser Technol. 146 (2022) 107604.

[18] K. Zhu, J.J. Xu, X.B. Wang, W. Li, K.S. Tian, Y.L. Hou, Chemical synthesis and coercivity enhancement of Nd2Fe14B nanostructures mediated by non-magnetic layer, Nano Res. 13 (2020) 1141–1148.

[19] D.J. Branagan, R.W. McCallum, Altering the cooling rate dependence of phase formation during rapid solidification in the Nd2Fe14B system, J. Magn. Magn. Mater. 146 (1995) 89–102.

[20] M. Sagawa, S. Hirosawa, H. Yamamoto, S. Fujimura, Y. Matsuura, Nd-Fe-B permant magnet materials, Jpn. J. Appl. Phys. 26 (1987) 785.

[21] D.S. Watring, J.T. Benzing, N. Hrabe, A.D. Spear, Effects of laser-energy density and build orientation on the structure–property relationships in as-built inconel 718 manufactured by laser powder bed fusion, Addit. Manuf. 36 (2020) 101425.

[22] A. Fujita, A Study on Magnetic Anisotropy Induced in the HDDR Process, DSC: DXN043700, Thesis (Ph.D.) 32, 1999, 32066494.

[23] D. Goll, F. Trauter, T. Bernthaler, J. Schanz, H. Riegel, G. Scheneider, Additive manufacturing of bulk nanocrystalline FeNdB based permanent magnets, Micromachines 12 (2021) 538.